Coherent Perfect Absorption of Arbitrary Wavefronts at an Exceptional Point

Helmut Hörner[1,*] Lena Wild[1] Yevgeny Slobodkin[2] Gil Weinberg[2] Ori Katz[2,†] and Stefan Rotter[1,‡]
[1]Institute for Theoretical Physics, TU Wien, Wiedner Hauptstraße 8-10/136, A-1040 Vienna, Austria
[2]Institute of Applied Physics, The Hebrew University of Jerusalem, 9190401, Jerusalem, Israel

(Received 5 April 2024; revised 23 July 2024; accepted 16 September 2024; published 22 October 2024)

A coherent perfect absorber exploits the interferometric nature of light to deposit all of a light field's incident energy into an otherwise weakly absorbing sample. The downside of this concept is that the necessary destructive interference in coherent perfect absorbers gets easily destroyed both by spectrally or spatially detuning the incoming light field. Each of these two limitations has recently been overcome by insights from exceptional-point physics and by using a degenerate cavity, respectively. Here, we show how these two concepts can be combined into a new type of cavity design, which allows broadband exceptional-point absorption of arbitrary wavefronts. We present two possible implementations of such a massively degenerate exceptional-point absorber and compare analytical results with numerical simulations.

DOI: 10.1103/PhysRevLett.133.173801

Introduction—While thin films or layers can only absorb a certain percentage of the light that shines through them in a single pass, an enhancement of absorption can be reached when the light beam has multiple passes through the absorbing material. This insight already indicates that placing an absorber in a cavity, where light bounces back and forth, can enhance the degree of absorption considerably [see Fig. 1(a) as an example]. The interferometric nature of light propagation in a cavity can boost the absorption even further—up to the point, where *all* the incoming light gets perfectly absorbed. In the single-mode case this phenomenon is known as "critical coupling" [1–5]. For multiple modes one speaks of "coherent perfect absorption," an effect that can also be interferometrically controlled through the relative phases of the incoming modes [6–13]. Conventional perfect absorbers have been widely explored in diverse platforms and applications, encompassing complex structures and disordered media [14–18], single-port interferometers [19,20], optical switches [21,22], sensors [23,24], and all-optical transistors and logic gates [25,26]. Recently, two of the major challenges of coherent perfect absorbers (CPAs) have been successfully addressed:

The first challenge is a CPA's narrow bandwidth, with slight frequency shifts disrupting the resonant absorption, typically resulting in a Lorentzian absorption profile. Research on how to make CPAs more broadband encompasses a wide array of approaches, such as metasurfaces [27–29], plasmonic effects [30–32], metallic nanoparticles metasurfaces [33], thin films [34], and broadband photonic crystal nanobeam resonators [35]. Recently, insights from exceptional point (EP) physics have also been used for advancing this goal [11–13]: at an EP, two (or more) discrete eigenvalues and eigenstates of a non-Hermitian system merge. Such an EP-CPA can be observed when two (or more) cavities with spectrally overlapping resonances are critically coupled, as depicted in Fig. 1(b). Specifically, it is possible to select system parameters such that both the critical-coupling condition, necessary for perfect absorption, and the EP condition coincide at the same real input frequency [11]. The result is a spectral degeneracy that leads to a significantly broadened (quartic) absorption spectrum [12,13], in analogy to the physics of white-light cavities [36–41] and of multimirror Fabry-Pérot interferometers [42].

The second major challenge concerns the limitation that a CPA typically only works for a well-defined input wavefront or mode. Detuning this input mode, e.g., in its incoming angle or phase profile, destroys the delicate interference necessary to achieve perfect absorption. To overcome this restriction, a massively degenerate (MAD) cavity turns out to be ideally suited [43], as illustrated in Fig. 1(c). In such a cavity, every incident light field is always imaged onto itself after each round-trip. This configuration thus enables the necessary interferometric CPA effect for any given spatial mode.

The question we explore here is whether these two distinct concepts can be integrated into a single CPA design that simultaneously achieves *spectral* and *spatial* degeneracy. Our approach to this new cavity design is based on the following considerations: a conventional CPA, as depicted in Fig. 1(a), can be transformed into a spectrally degenerate CPA by critically coupling it to another cavity, as illustrated in Fig. 1(b). Similarly, the same conventional CPA can be transformed into a spatially degenerate CPA by

*Contact author: helmut.hoerner@tuwien.ac.at
†Contact author: orik@mail.huji.ac.il
‡Contact author: stefan.rotter@tuwien.ac.at

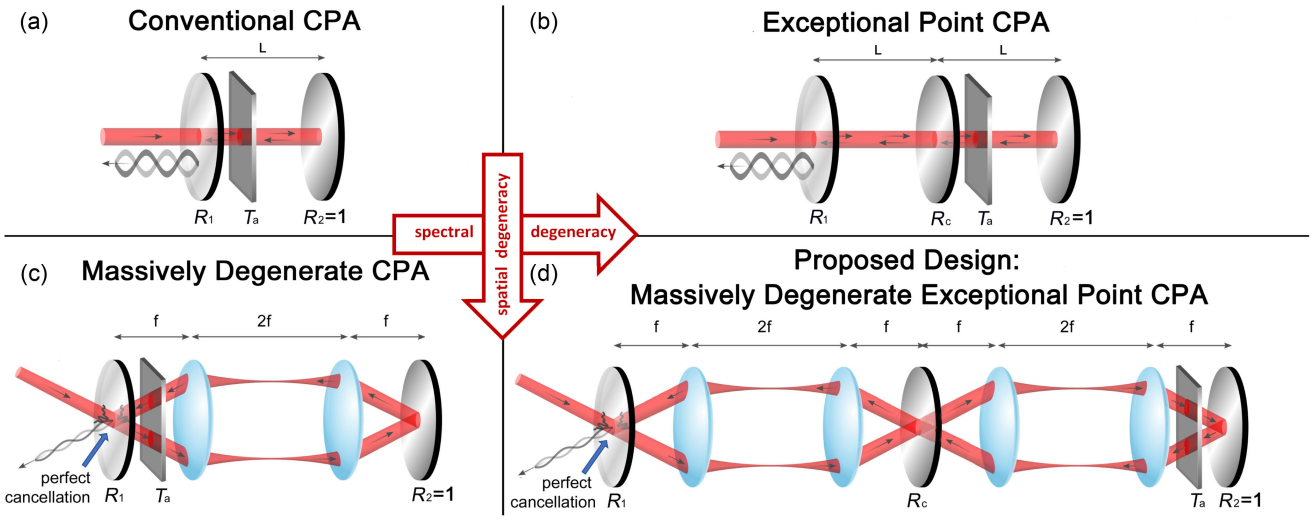

FIG. 1. (a) A conventional CPA (critically coupled cavity). When the critical-coupling condition $R_1 = T_a^2$ is met, the incident coherent light field is perfectly absorbed, but only for a single plane-wave input mode at the right frequency. (b) A spectrally degenerate EP-CPA, consisting of two weakly coupled conventional CPAs. When the critical-coupling conditions $R_c = 4R_1/(1+R_1)^2$ and $R_1 = T_a^2$ are met, the (generally distinct) resonance points merge at a single, real frequency. This spectral degeneracy results in a broadened (quartic) absorption spectrum (not shown). (c) A MAD-CPA is a spatially degenerate extension of the conventional CPA: because of the self-imaging telescopic lens arrangement, any incoming spatial mode is mapped onto itself after each round-trip, leading to perfect cancellation of any back-reflected light at the front mirror. (d) The MAD-EP-CPA ("Design A") combines the features of spatial and spectral degeneracies for improved spatial and spectral acceptance.

incorporating two lenses (focal length f) in a telescopic configuration (of length $4f$), as illustrated in Fig. 1(c). Thus, merging these two ideas by critically coupling two spatially degenerate cavities, as illustrated in Fig. 1(d), should result in a CPA that is both spatially and spectrally degenerate.

Spatial and spectral degeneracy—To derive the reflection behavior of light incident from the left on this MAD-EP-CPA we employ a scalar optics model for polarized light, considering a large, yet finite, number of spatial modes. Let $\mathbf{R}_1$, $\mathbf{R}_2$, and $\mathbf{R}_c$ represent the reflection matrices, and $\mathbf{T}_1$, $\mathbf{T}_2$, and $\mathbf{T}_c$ the transmission matrices for the left, right, and central mirror, respectively. Additionally, $\mathbf{T}_a$ is the transmission through the absorber and $\mathbf{T}_{4f}$ represents the transmission matrix for propagation through a $4f$ system, comprising two lenses in a telescopic configuration (without mirrors or absorbers). $\mathbf{T}_{4f}$ acts as a double Fourier transform producing a spatially flipped image and a phase shift $e^{i\phi}$ that is the same for all modes. Using that the same reflection and transmission coefficients apply to all modes at the mirrors and the absorber, all matrices except $\mathbf{T}_{4f}$ become diagonal matrices, e.g., $\mathbf{R}_1 = r_1\mathbb{1}$, $\mathbf{T}_1 = t_1\mathbb{1}$, etc. Using a transfer matrix approach, we can construct from these individual transmission matrices the sought-after reflection matrix $\mathbf{R}_{\mathrm{CPA}}^{(\mathrm{A})}$ for the entire MAD-EP-CPA [[44], S1] [Design A in Fig. 1(d)],

$$\mathbf{R}_{\mathrm{CPA}}^{(\mathrm{A})} = \frac{t_a^2\mathbf{T}_{4f}^4 + r_c(1+r_1t_a^2)\mathbf{T}_{4f}^2 + r_1\mathbb{1}}{r_1t_a^2\mathbf{T}_{4f}^4 + r_c(r_1+t_a^2)\mathbf{T}_{4f}^2 + \mathbb{1}}. \tag{1}$$

The matrix $\mathbf{T}_{4f}^2$ in Eq. (1) results in a quadruple Fourier transformation with a uniform phase shift $e^{2i\phi}$ for all modes and can thus be represented as a simple diagonal matrix $\mathbf{T}_{4f}^2 = e^{2i\phi}\mathbb{1}$. Analogously, $\mathbf{T}_{4f}^4 = e^{4i\phi}\mathbb{1}$, turning $\mathbf{R}_{\mathrm{CPA}}^{(\mathrm{A})}$ into a diagonal matrix with identical entries $r_{\mathrm{CPA}}(\omega)$ along the diagonal. Therefore, Eq. (1) can be reduced to a simple scalar equation, which proves that all modes are subject to the same reflection behavior in the system (*spatial* degeneracy). The function $r_{\mathrm{CPA}}(\omega)$ is determined by the power reflectivities $R_1 = |r_1|^2$, $R_c = |r_c|^2$ of the mirrors, and by the absorber's one-way transmissivity $T_a = |t_a|^2$. To determine the conditions for *spectral* degeneracy, i.e., for the EP to occur at a real frequency, the values R_1, R_c, and T_a need to be adjusted such that the two solutions ω_1, ω_2 of the equation $r_{\mathrm{CPA}}(\omega) = 0$ merge into a single real-valued frequency ω. These conditions are

$$R_1 = T_a^2 \quad \text{and} \quad R_c = \frac{4R_1}{(1+R_1)^2}. \tag{2}$$

A detailed derivation is available in the Supplemental Material [[44], S1–S3]. The result (2) shows that the relationship between T_a and R_1 for a MAD-EP-CPA is identical to that of a single-cavity MAD-CPA [43]: the higher the reflectivity R_1 of the input-coupling mirror, the weaker the internal absorber needs to be. Additionally, the relation between R_c and R_1 indicates that R_c quickly approaches values near 1 with increasing values of R_1, indicating weak coupling between the left and right subcavity.

Numerical simulations—To corroborate that these analytical results are, indeed, applicable to the multimode MAD-EP-CPA, and to assess the impact of deviations in certain system parameters (such as minor misalignments of the mirrors), we conducted detailed numerical simulations. In these simulations, light propagation through and reflection from each optical element, as well as the propagation between optical elements, were realistically simulated using scalar Fourier wave optics methods, as described, e.g., in [49–51]. Based on these simulations, reflection and transmission matrices were calculated for each element. These matrices were then used to construct the corresponding scattering and transfer matrices. Finally, a transfer matrix approach was employed to simulate the complex behavior of the coupled cavities forming the CPAs. As incident field directly adjacent to the outer surface of the input coupling lens R_1, we used a random speckle field [Fig. 2(a)] generated by 5000 Fourier modes with equal amplitude and random phase, with k-vector angles uniformly and randomly distributed between 0° and 2°. The intensity profile of the reflected field is also taken at that position. A discussion of all basic simulation parameters

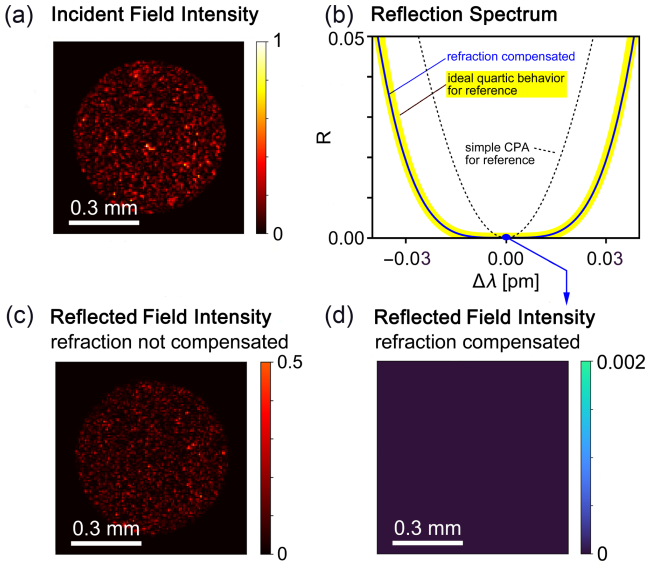

FIG. 2. Numerical simulation of the proposed MAD-EP-CPA, as depicted in Fig. 1(d). (a) Intensity pattern of a simulated complex incident random speckle field directly adjacent to the outer surface of R_1, composed of 5000 modes. (b) Reflection spectrum across the entire field of view with compensation of the refraction aberrations caused by the absorber with thickness 0.6 mm (blue line). For reference, ideal quartic behavior is shown with a thick yellow line, and a conventional CPA with the same absorber with a black dotted line. (c) Reflected field intensity pattern taken directly adjacent to the outer surface of R_1 at the resonance point when the refraction in the absorber is not compensated. (d) Reflected field intensity pattern at the resonance point with refraction compensated. (Simulation parameters: $R_1 = 0.7$, $R_c = 0.968\,86$. $T_a = \sqrt{0.7}$, wavelength: around the resonance point near $\lambda = 633$ nm, focal length $f = 25$ mm).

can be found in Sec. S4 of the Supplemental Material [44]. Without compensating for the refractive index of the absorber (assumed to be $n_r = 1.5$ with a thickness of $d = 0.6$ mm), our numerical simulation shows that the minimal field-of-view reflectivity does not drop below 66% with the given parameters [see Fig. 2(c)]. To address this, we adjusted the focal length of the rightmost lens in Fig. 1(d) to $f' = f - d(n_r - 1/n_r)/2$. This adjustment compensates for the increased optical path length caused by the absorber and preserves identical optical path lengths in both the left and right subcavity. As shown in the numerically calculated reflection spectrum of Fig. 2(b) (blue line), this correction restores perfect absorption at the point of degeneracy and verifies the successful operation of our MAD-EP-CPA cavity design [see the broad yellow line in Fig. 2(b) for comparison with an ideal quartic absorption line shape]. For a more detailed explanation of this refraction compensation technique, readers are referred to the Supplemental Material [[44], S9]. Another potential strategy to minimize refractive aberrations is to use an absorber with a refractive index whose real part is as close to 1 as possible [52].

The numerical simulations also allow us to study the impact of small deviations from optimal system parameters, and help to pinpoint the critical system parameters influencing the system performance. For instance, the simulations demonstrate that the system exhibits robustness to deviations of the optimal reflectivity R_1 of the input coupling mirror (to within about ±5%), or of the optimal transmissivity T_a of the absorber (to within about ±2%). In contrast, deviations in the reflectivity R_c of the central coupling mirror from its optimal value significantly affect the system performance. Even a mere 1% deviation from the optimal value results in a minimum reflectivity of approximately 5%, significantly diminishing the system's absorption efficiency (further details can be found in the Supplemental Material [[44], S4]). As expected, the precise parallel alignment of the mirrors is also crucial, particularly for the central coupling mirror, as shown in Fig. 3. Further information on crucial parameters, like the effects of minor variations in the alignment of the two cavity lengths, can be found in the Supplemental Material [[44], S4]. This section also examines the impact of residual reflections from lenses by simulating commercially available lenses with 633 nm V coating. Our simulations indicate that, with such lenses, the MAD-EP-CPA maintains a minimum power reflectivity of 0.5%, and the characteristic broadening of the reflection spectrum remains evident.

Considerations for larger k-vector angles—Computational constraints restrict the k-vector angles in our simulations to a range of 0° to 2°. Our analysis suggests, however, that our design remains effective even for significantly larger angles: assuming the use of aspherical, perfect lenses, equal optical path lengths for all round-trip

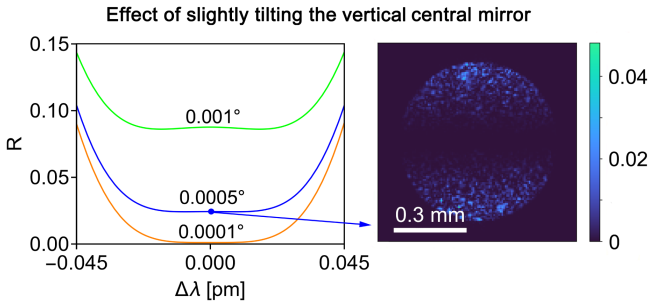

FIG. 3. Sensitivity to misalignment of the central coupling mirror (same simulation parameters as in Fig. 2). Left: reflection spectrum across the entire field of view when the center mirror is slightly tilted out of the vertical alignment. Right: reflected field intensity pattern taken directly adjacent to the outer surface of R_1 when the central mirror is tilted by 0.0005°. Perfect absorption now only occurs in a narrow horizontal area along the tilt axis.

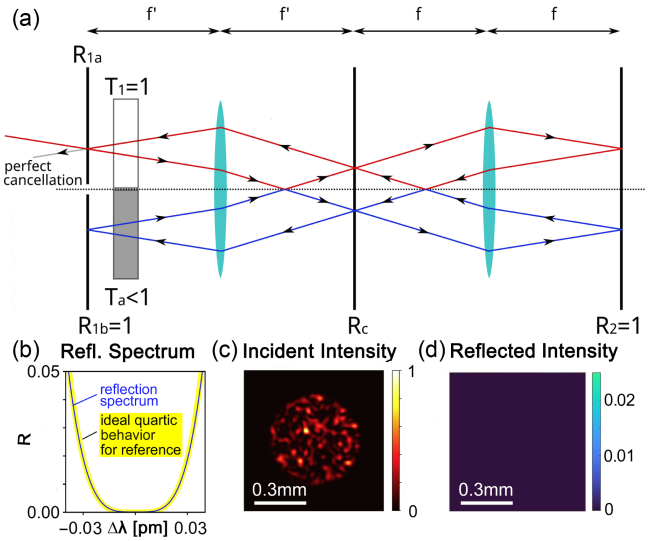

FIG. 4. Alternative MAD-EP-CPA configuration ("Design B"). (a) Rather than coupling two $4f$ cavities as in Design A, a coupling mirror (R_c) is positioned at the center of a single $4f$ cavity. The left mirror is divided into an input-coupling part (R_{1a}) illustrated above the optical axis, and a completely reflecting mirror (R_{1b}) depicted below the optical axis. The absorber with transmissivity T_a is placed next to mirror R_{1b}. To correct for refraction aberrations, the left len's focal length is adjusted to f', and a transparent slab T_1, matching T_a in thickness and real value of refractive index, is placed near R_{1a}. Exemplary beam paths are marked in red and blue above and below the optical axis. (b) Numerical simulation of the field-of-view reflection spectrum (blue line) in comparison to an ideal quartic behavior (broad yellow line). (c) Incident field intensity pattern directly adjacent to the outer surface of R_{1a}, consisting of 5000 random modes. (d) Reflected field intensity pattern adjacent to the outer surface of R_{1a}, demonstrating perfect absorption.

trajectories are maintained for all k-vector angles. The only conceptual limitation then arises from our mechanism for compensating refraction aberrations in the absorber, as described in the Supplemental Material [[44], S9]. Because of the paraxial approximation used, this method becomes less effective for angles $\gtrsim 10°$, necessitating a more refined compensation mechanism.

Higher order MAD-EP-CPAs—We have also studied MAD-EP-CPA systems encompassing more than two coupled cavities, as detailed in the Supplemental Material [[44], S6]. Interestingly, constructing an EP-CPA with an increasing number of cavities results in a reflection spectrum around the resonance frequencies akin to a Butterworth bandpass filter, a concept from electrical filter theory [53,54]. This observation is consistent with the established understanding that, as outlined in [42], the Butterworth function also characterizes the transmission behavior of a multimirror Fabry-Pérot interferometer in the absence of a dissipative element.

Alternative implementation—The initial design for a MAD-EP-CPA ("Design A"), as discussed thus far and illustrated in Fig. 1(d), is probably the most obvious solution for merging the concepts shown in Figs. 1(b) and 1(c).

However, Design A poses challenges in the implementation, as it involves weakly coupling two plane-parallel cavities with altogether four embedded lenses. We thus propose in Fig. 4(a) an alternative "Design B," involving a coupling mirror with reflectivity R_c at the center of a *single* $4f$ cavity, requiring only two lenses. This simplification requires a division of the left mirror at the optical axis into an input-coupling segment with reflectivity $R_{1a} < 1$ and a fully reflective mirror $R_{1b} = 1$. The weak absorber is then placed adjacent to the totally reflective mirror R_{1b}. Additionally, to mitigate the additional refraction introduced by the absorber, we adjust the focal length of the left lens to $f' = f - d(n_r - 1/n_r)/2$ (see Supplemental Material [[44], S9]). Furthermore, to ensure an identical optical path length above and below the optical axis, we have incorporated a transparent slab, designated T_1, having the same thickness and refractive index as the absorber, adjacent to mirror R_{1b}. Design B can be seen as a "folded-up" variant of Design A by identifying analogous round-trip paths. For instance, in Design A, light undergoes self-imaging round-trips within the right subcavity, with a corresponding path in Design B from the bottom left to the top right. A similar parallel can be observed for round-trips in Design A's left subcavity, corresponding with the path from top left to bottom right in Design B. In both of these scenarios, a *single reflection* at Design A's central mirror is substituted by *two transmissions* through Design B's central mirror. Also, for the third round-trip path in Design A, where light propagates between the farthest mirrors R_1 and R_2, an analog round-trip path can be identified in Design B (see Supplemental Material [[44], S8] for details). However, it is crucial to recognize that such comparisons between Design A and Design B offer, at best, a qualitative analogy. A comprehensive comparison requires a sound mathematical analysis, considering the

infinite sum of all possible round-trips and the effects of coupling between the two subcavities. Nonetheless, this qualitative comparison hints that the condition for the *transmissivity* T_c of the central mirror in Design B may resemble the condition for the *reflectivity* R_c of the central mirror in Design A. Using an analogous derivation method as before, the following matrix equation for $\mathbf{R}_{\mathrm{CPA}}^{(\mathrm{B})}$ can be established:

$$\mathbf{R}_{\mathrm{CPA}}^{(\mathrm{B})} = \frac{t_a^2 \mathbf{T}_{2f}^8 + (1 + r_{1a} t_a^2 - a)\mathbf{T}_{2f}^4 + r_{1a}\mathbb{1}}{r_{1a} t_a^2 \mathbf{T}_{2f}^8 + (r_{1a} + t_a^2 - a)\mathbf{T}_{2f}^4 + \mathbb{1}}, \tag{3}$$

with the scalar value $a = r_c^2(t_a^2 + 1)(r_{1a}^2 + 1)$. Observe how the structure of Eq. (3) resembles the structure of Eq. (1). Because $\mathbf{T}_{2f}^4 = \mathbf{T}_{4f}^2$, the matrix $\mathbf{T}_{2f}^4$ in Eq. (3) results in a quadruple Fourier transformation with a uniform phase shift $e^{2i\phi}$ for all modes, and can thus be represented as a simple diagonal matrix $\mathbf{T}_{4f}^2 = e^{2i\phi}\mathbb{1}$. Analogously, $\mathbf{T}_{2f}^8 = e^{4i\phi}\mathbb{1}$. Consequently, $\mathbf{R}_{\mathrm{CPA}}^{(\mathrm{B})}$ becomes a diagonal matrix and can be reduced to a simple scalar equation, which proves the *spatial* degeneracy of Design B. The *spectral* degeneracy condition can be met when the following EP conditions are fulfilled (see Supplemental Material [[44], S7]):

$$R_{1a} = T_a^2 \tag{4}$$

$$R_c = \left(\frac{1 - T_a}{1 + T_a}\right)^2 \Rightarrow T_c = \frac{4T_a}{(1 + T_a)^2}. \tag{5}$$

Note the similarity between Eqs. (4), (5), and (2). While the central mirror in Design A must exhibit *high reflectivity* at the exceptional point (EP), in Design B it requires *high transmissivity*, which is in accordance with our earlier qualitative analysis. The analytical results confirm the anticipated quartic behavior and have been corroborated by numerical computer simulations, as illustrated in Fig. 4.

Conclusions—We have introduced two CPA designs that combine spectral and spatial degeneracy. Through analytical and numerical models, we have validated the feasibility of this concept and explored its limitations. This new type of CPA is capable of perfectly depositing a light beam in a weak absorber over a wider spectral range as compared to a conventional CPA and regardless of the light beam's spatial wavefront.

Acknowledgments—We would like to express our gratitude to Maximilian Prüfer (TU Wien), Jacob Scheuer (Tel Aviv University), and Birgitta Schultze-Bernhardt (TU Graz) for very helpful discussions. The numerical calculations were performed on the Vienna Scientific Cluster (VSC). This project was supported by the H2020 European Research Council (101002406).

[1] R. B. Adler, L. J. Chu, and R. M. Fano, *Electromagnetic Energy Transmission and Radiation*, 5th ed., The MIT Press Classics (MIT Press, Cambridge, Mass.[u.a.], 1969).
[2] H. A. Haus, *Waves and Fields in Optoelectronics*, Prentice-Hall Series in Solid State Physical Electronics (Prentice-Hall, Englewood Cliffs, NJ, 1984).
[3] M. L. Gorodetsky and V. S. Ilchenko, Optical microsphere resonators: Optimal coupling to high-q whispering-gallery modes, J. Opt. Soc. Am. B **16**, 147 (1999).
[4] M. Cai, O. Painter, and K. J. Vahala, Observation of critical coupling in a fiber taper to a silica-microsphere whispering-gallery mode system, Phys. Rev. Lett. **85**, 74 (2000).
[5] A. Yariv, Critical coupling and its control in optical waveguide-ring resonator systems, IEEE Photonics Technol. Lett. **14**, 483 (2002).
[6] Y. D. Chong, L. Ge, H. Cao, and A. D. Stone, Coherent perfect absorbers: Time-reversed lasers, Phys. Rev. Lett. **105**, 053901 (2010).
[7] Y. D. Chong and A. D. Stone, Hidden black: Coherent enhancement of absorption in strongly scattering media, Phys. Rev. Lett. **107**, 163901 (2011).
[8] D. G. Baranov, A. Krasnok, T. Shegai, A. Alù, and Y. Chong, Coherent perfect absorbers: Linear control of light with light, Nat. Rev. Mater. **2**, 17064 (2017).
[9] K. Kishino, M. Unlu, J.-I. Chyi, J. Reed, L. Arsenault, and H. Morkoc, Resonant cavity-enhanced (RCE) photodetectors, IEEE J. Quantum Electron. **27**, 2025 (1991).
[10] M. S. Ünlü, K. Kishino, H. J. Liaw, and H. Morkoç, A theoretical study of resonant cavity-enhanced photodectectors with Ge and Si active regions, J. Appl. Phys. **71**, 4049 (1992).
[11] W. R. Sweeney, C. W. Hsu, S. Rotter, and A. D. Stone, Perfectly absorbing exceptional points and chiral absorbers, Phys. Rev. Lett. **122**, 093901 (2019).
[12] C. Wang, W. R. Sweeney, A. D. Stone, and L. Yang, Coherent perfect absorption at an exceptional point, Science **373**, 1261 (2021).
[13] S. Soleymani, Q. Zhong, M. Mokim, S. Rotter, R. El-Ganainy, and Ş. K. Özdemir, Chiral and degenerate perfect absorption on exceptional surfaces, Nat. Commun. **13**, 599 (2022).
[14] X. Jiang, S. Yin, H. Li, J. Quan, H. Goh, M. Cotrufo, J. Kullig, J. Wiersig, and A. Alù, Coherent control of chaotic optical microcavity with reflectionless scattering modes, Nat. Phys. **20**, 109 (2023).
[15] W. R. Sweeney, C. W. Hsu, and A. D. Stone, Theory of reflectionless scattering modes, Phys. Rev. A **102**, 063511 (2020).
[16] A.-S. B.-B. Dhia, L. Chesnel, and V. Pagneux, Trapped modes and reflectionless modes as eigenfunctions of the same spectral problem, Proc. R. Soc. A **474**, 20180050 (2018).
[17] M. Horodynski, M. Kühmayer, C. Ferise, S. Rotter, and M. Davy, Anti-reflection structure for perfect transmission through complex media, Nature (London) **607**, 281 (2022).
[18] K. Pichler, M. Kühmayer, J. Böhm, A. Brandstötter, P. Ambichl, U. Kuhl, and S. Rotter, Random anti-lasing through coherent perfect absorption in a disordered medium, Nature (London) **567**, 351 (2019).

[19] S. Li, J. Luo, S. Anwar, S. Li, W. Lu, Z. H. Hang, Y. Lai, B. Hou, M. Shen, and C. Wang, An equivalent realization of coherent perfect absorption under single beam illumination, Sci. Rep. **4**, 7369 (2014).
[20] Y. Jin and K. Yu, Broadband single-channel coherent perfect absorption with a perfect magnetic mirror, Opt. Express **28**, 35108 (2020).
[21] A. Mock, Low-power all-optical switch based on time-reversed microring laser, IEEE Photonics J. **4**, 2229 (2012).
[22] M.-D. Guo, H.-F. Li, F.-L. Wang, C.-X. Zhou, and Y.-J. Wu, Nonlinear optical switch based on coherent perfect absorption, Opt. Lett. **48**, 4037 (2023).
[23] C. Li, J. Qiu, J.-Y. Ou, Q. H. Liu, and J. Zhu, High-sensitivity refractive index sensors using coherent perfect absorption on graphene in the vis-NIR region, ACS Appl. Nano Mater. **2**, 3231 (2019).
[24] Y. Zhang, F.-P. Wu, and H.-F. Zhang, Theoretical model of a RI THz sensor realized by coherent perfect absorption with optical phase modulation, IEEE Sensors J. **22**, 14842 (2022).
[25] R. Ebrahimi Meymand, A. Soleymani, and N. Granpayeh, All-optical AND, OR, and XOR logic gates based on coherent perfect absorption in graphene-based metasurface at terahertz region, Opt. Commun. **458**, 124772 (2020).
[26] X. Fang, K. F. MacDonald, and N. I. Zheludev, Controlling light with light using coherent metadevices: All-optical transistor, summator and invertor, Light Sci. Appl. **4**, e292 (2015).
[27] T. Guo and C. Argyropoulos, Tunable and broadband coherent perfect absorption by ultrathin black phosphorus metasurfaces, J. Opt. Soc. Am. B **36**, 2962 (2019).
[28] Z. Zhang, Q. Xie, L. Guo, C. Su, M. Wang, F. Xia, J. Sun, K. Li, H. Feng, and M. Yun, Dual-controlled tunable dual-band and ultra-broadband coherent perfect absorber in the THz range, Opt. Express **30**, 30832 (2022).
[29] H. Zhang and H. Zhang, Ultra-broadband coherent perfect absorption via elements with linear phase response, Opt. Express **30**, 37350 (2022).
[30] M. Pu, Q. Feng, M. Wang, C. Hu, C. Huang, X. Ma, Z. Zhao, C. Wang, and X. Luo, Ultrathin broadband nearly perfect absorber with symmetrical coherent illumination, Opt. Express **20**, 2246 (2012).
[31] L. Baldacci, S. Zanotto, G. Biasiol, L. Sorba, and A. Tredicucci, Interferometric control of absorption in thin plasmonic metamaterials: General two port theory and broadband operation, Opt. Express **23**, 9202 (2015).
[32] C. Wang, X. Shen, H. Chu, J. Luo, X. Zhou, B. Hou, R. Peng, M. Wang, and Y. Lai, Realization of broadband coherent perfect absorption of spoof surface plasmon polaritons, Appl. Phys. Lett. **120**, 171703 (2022).
[33] H. Noh, S. M. Popoff, and H. Cao, Broadband subwavelength focusing of light using a passive sink, Opt. Express **21**, 17435 (2013).
[34] S. Li, J. Luo, S. Anwar, S. Li, W. Lu, Z. H. Hang, Y. Lai, B. Hou, M. Shen, and C. Wang, Broadband perfect absorption of ultrathin conductive films with coherent illumination: Superabsorption of microwave radiation, Phys. Rev. B **91**, 220301(R) (2015).
[35] J. Choi, Y. K. Hong, and H. Noh, Coherent perfect loss with single and broadband resonators at photonic crystal nanobeam, Nanophotonics **13**, 377 (2024).
[36] A. Wicht, K. Danzmann, M. Fleischhauer, M. Scully, G. Müller, and R.-H. Rinkleff, White-light cavities, atomic phase coherence, and gravitational wave detectors, Opt. Commun. **134**, 431 (1997).
[37] H. N. Yum, Y. J. Jang, X. Liu, and M. S. Shahriar, Visualization of superluminal pulses inside a white light cavity using plane wave spatio temporal transfer functions, Opt. Express **20**, 18898 (2012).
[38] G. S. Pati, M. Salit, K. Salit, and M. S. Shahriar, Demonstration of a tunable-bandwidth white-light interferometer using anomalous dispersion in atomic vapor, Phys. Rev. Lett. **99**, 133601 (2007).
[39] D. D. Smith, K. Myneni, J. A. Odutola, and J. C. Diels, Enhanced sensitivity of a passive optical cavity by an intracavity dispersive medium, Phys. Rev. A **80**, 011809 (R) (2009).
[40] D. D. Smith, H. Chang, L. Arissian, and J. C. Diels, Dispersion-enhanced laser gyroscope, Phys. Rev. A **78**, 053824 (2008).
[41] O. Kotlicki and J. Scheuer, Wideband coherent perfect absorber based on white-light cavity, Opt. Lett. **39**, 6624 (2014).
[42] H. van de Stadt and J. M. Muller, Multimirror fabry–perot interferometers, J. Opt. Soc. Am. A **2**, 1363 (1985).
[43] Y. Slobodkin, G. Weinberg, H. Hörner, K. Pichler, S. Rotter, and O. Katz, Massively degenerate coherent perfect absorber for arbitrary wavefronts, Science **377**, 995 (2022).
[44] See Supplemental Material at http://link.aps.org/supplemental/10.1103/PhysRevLett.133.173801 for coherent perfect absorption of arbitrary wavefronts at an exceptional point, which includes Refs. [42,45–48].
[45] J. Frei, X.-D. Cai, and S. Muller, Multiport s-parameter and t-parameter conversion with symmetry extension, IEEE Trans. Microwave Theory Tech. **56**, 2493 (2008).
[46] A. E. Siegman, *Lasers (Revised)* (University Science Books, 1986).
[47] F. A. Graybill, *Matrices with Applications in Statistics* (Wadsworth International Group, Belmont, California, 1983).
[48] T.-T. Lu and S.-H. Shiou, Inverses of 2×2 block matrices, Comput. Math. Appl. **43**, 119 (2002).
[49] D. Voelz, *Computational Fourier Optics: A MATLAB Tutorial* (SPIE Press, Bellingham, Wash, 2011).
[50] D. G. Voelz and M. C. Roggemann, Digital simulation of scalar optical diffraction: Revisiting chirp function sampling criteria and consequences, Appl. Opt. **48**, 6132 (2009).
[51] J. Schmidt, *Numerical Simulation of Optical Wave Propagation with Examples in MATLAB*, Press Monograph No. v.PM199 (Society of Photo-Optical Instrumentation Engineers (SPIE), Bellingham, 2010) description based on publisher supplied metadata and other sources.
[52] C. Tao, X. Zou, K. Du, L. Zhang, H. Yan, and X. Yuan, Ultralow-refractive-index optical thin films built from shape-tunable hollow silica nanomaterials, Opt. Lett. **43**, 1802 (2018).
[53] V. K. Aatre, *Network Theory And Filter Design* (New Age International Publishers, New Delhi, 2014).
[54] S. Butterworth, On the theory of filter amplifiers, in *Experimental Wireless & the Wireless Engineer* (London, 1930), Vol. 7, p. 536.